Computers and Concrete, *Vol. 24, No. 1 (2019) 51-61*
DOI: https://doi.org/10.12989/cac.2019.24.1.051

A cohesive model for concrete mesostructure considering friction effect between cracks

Yi-qun Huang[1a] and Shao-wei Hu[*2]

[1]*College of Mechanics and Materials, Hohai University, 1 Xikang Road, Nanjing, China*
[2]*School of Civil Engineering, Chongqing University, 174 Shazheng Road, Chongqing, China*

(Received July 15, 2018, Revised April 12, 2019, Accepted May 17, 2019)

Abstract. Compressive ability is one of the most important mechanical properties of concrete material .The compressive failure process of concrete is pretty complex with internal tension, shear damage and friction between cracks. To simulate the complex fracture process of concrete at meso level, methodology for meso-structural analysis of concrete specimens is developed; the zero thickness cohesive elements are pre-inserted to simulate the crack initiation and propagation; the constitutive applied in cohesive element is established to describe the mechanism of crack separation, closure and friction behavior between the fracture surfaces. A series of simulations were carried out based on the model proposed in this paper. The results reproduced the main fracture and mechanical feature of concrete under compression condition. The effect of key material parameters, structure size, and aggregate content on the concrete fracture pattern and loading carrying capacities was investigated. It is found that the inner friction coefficient has a significant influence on the compression character of concrete, the compression strength raises linearly with the increase of the inner friction coefficient, and the fracture pattern is sensitive to the mesostructure of concrete.

Keywords: concrete; mesostructure; fracture pattern; constitutive; cohesive element; friction

1. Introduction

Concrete is a composite material consisting of aggregates, cement matrix and interface transition zone (ITZ). The macro mechanical behavior of concrete is determined by its mesoscopic components. Therefore, researches about concrete mutil-scale simulation have been widely carried out to reveal the meso, macro-scale mechanism of concrete.

In the traditional concrete simulation studies, researchers mainly used the continuum solid elements (Mohamed and Will 1999, Wriggers and Moftah 2006, Zhang *et al*. 2015) or lattice elements (Van Mier *et al.* 2002, Lilliu and Van Mier 2003, Grassl *et al.* 2012) to discretize the components (aggregates, mortar, ITZ) of concrete, crack initiation and propagation of concrete were represented using the deletion of failure elements (Shen *et al.* 2015, Chen *et al.* 2015) or remeshing at the crack tip (Wang *et al.* 2000). Other new methods such as Meso element equivalent method (MEEM) (Jin *et al*. 2012, Du *et al.* 2013a, b), by averaging the material properties of each component in the element, was used to simulate the macroscopic mechanical character of concrete without representing the expansion of cracks. Other methods such as extended finite element method (XFEM), using the improved shape function to avoid elements remeshing or deletion when crack propagation occur, was used to analyze the fracture character of concrete lately (Roth *et al.* 2015). Also, the discrete element method (DEM) was adopted to simulate the fracture process (Haeri and Sarfarazi 2016, Rangari *et al*. 2018, Haeri *et al.* 2018, Nguyen *et al*. 2019) by using the separated elements (such as particle flow) to discrete the concrete mesostructure.

Recently, with the invention of the cohesive element, some researchers used this element to simulate cracking and separation of concrete (Caballero *et al.* 2006, López *et al.* 2008a, b, Ooi and Yang 2011, Snozzi *et al.* 2011, Li and Chen 2017). The cohesive element is a transitional element between solid elements, its geometry thickness can be set to any non-negative value including zero. So cohesive element can characterize the ITZ and potential cracks in concrete. There are only normal stress and shear stress existing in the cohesive element which make the element be suitable for describing the mechanical behavior of concrete cracks. Recently, researches (Yang *et al.* 2009, Wang *et al.* 2015, Wang *et al.* 2016) show that the element size of concrete structure with cohesive elements has little effect on fracture pattern and macro mechanical response of concrete, so the cohesive element could adapt to various sizes of concrete structures. Current researches about cohesive element mainly focus on the tensile and shear fracture characteristic of concrete. However, the compression fracture characteristic is also an important mechanical indicator for concrete. The fracture mode and mechanical behavior under compression condition is more complex in contrast to one under tensile and shear condition, especially the interaction force between the cracks (normal compression stress, shear

∗Corresponding author, Professor
E-mail: hushaowei@nhri.cn
[a]Ph.D. Candidate
E-mail: yiqunhuang@hhu.edu.cn

http://www.techno-press.org/?journal=cac&subpage=8 ISSN: 1598-8198 (Print), 1598-818X (Online)

Table 1 The size distribution of aggregates in experiment done by Van Vliet and Van Mier (1996)

Grain size (mm)	Unit content (kg/m^3)	Volume content (%)
8~4	540	19.29
4~2	363	12.91
2~1	272	9.71
1~0.5	272	9.71
0.5~0.25	234	8.35

stress, and friction stress when cracks closed) has a significant effect on compression characteristic.

Many numerical methods have been presented to investigate the fracture behavior of concrete mesostructure under compression condition, including the tradition FEM model with the application of concrete damage plastic model (Shen *et al.* 2015, Jin *et al*. 2019), the lattice model with the constitutive considering the tensile and compression fracture (Guan *et al*. 2018, Karavelić *et al*. 2019). However, these two methods all used the macro tensile and compression constitutive to characterize the fracture behavior of the concrete meso structure, without considering the effects of shear damage and friction. In addition, the DEM method was also used to simulate the fracture behavior of concrete meso-structure under compression condition (Rangari *et al*. 2018, Nguyen *et al*. 2019). The DEM method could roughly reproduced the failure process of concrete, but this method has a difficulty to quantitatively analyze the opening degree and dislocation of cracks.

In this paper, we present a numerical model to analyze the complex fracture characteristic of concrete. In this model, pre-inserted zero thickness cohesive elements were adopted to generate the concrete meso-structure, and a constitutive governing the cohesive element was established to describe the normal/shear stress and the friction inside the fracture surfaces. The proposed model was solved in ABAQUS with subroutine VUMAT. The simulation results were comprehensively analyzed to investigate the influence of key parameters, which may help improving design of concrete structures.

2. Numerical model

2.1 Generation of concrete mesostructure

A random polygon aggregates generation algorithm including polygon generation and aggregates overlap check was adopted in this paper based on the work done by Gao and Liu (2003), Du and Sun (2007). The central idea of algorithm is to generate random aggregates in a repeated manner, until the target area of aggregates is achieved.

The aggregates size distribution in the work done by Van Vliet and Van Mier (1996) is adopted in this paper. Assuming the density of aggregate is 2800 kg/m^3, the size distribution is listed in Table 1. For simplicity, only coarse aggregates larger than 2 mm are considered in this study. The typical numerical model of concrete mesostructure is shown as in Fig. 1.

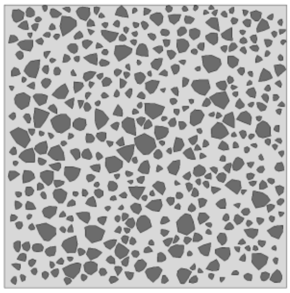

Fig. 1 Typical numerical model of concrete mesostructure

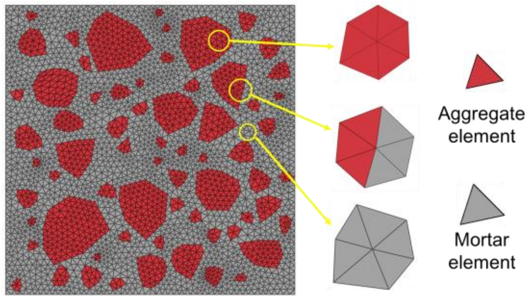

(a) Initial mesh

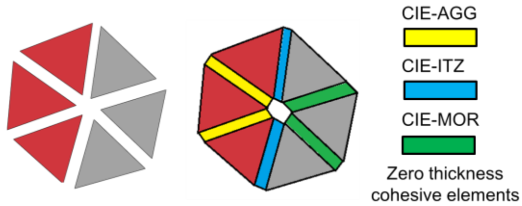

(b) Separation of the solid elements and insertion of the cohesive elements

Fig. 2 Insertion of cohesive elements

2.1 Insertion of cohesive elements

After the numerical model being meshed by solid element, the zero thickness cohesive interface elements (CIEs or cohesive element) with 4 nodes are inserted into the interfaces between the solid elements. The cohesive elements are adopted to represent the ITZ and potential cracks. The inserting method of cohesive elements can be mainly performed by following three steps:

Step1: Separate the solid elements and renumber the nodes in all elements;

Step2: Insert the cohesive elements between the solid elements;

Step3: Classify the cohesive elements based on the type of solid elements on each side of the cohesive element.

There are three kinds of CIE in the model: CIE-AGG as the CIEs inside the aggregates, CIE-MOR as the potential cracks inside the mortar, CIE-ITZ as the interfaces between the aggregates and mortar. The process of the insertion of CIEs is shown in Fig. 2.

3. Constitutive behavior of cohesive element

The constitutive used in cohesive elements is represented by the relation between the traction and

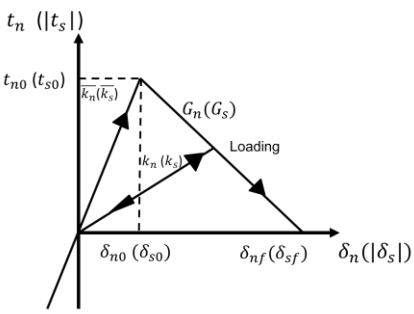

Fig. 3 Bilinear damage model

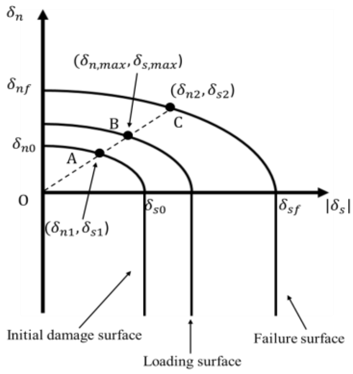

Fig. 4 Damage surfaces for the cohesive element

displacement. The traction containing normal stress t_n and shear stress t_s, and displacements containing normal displacement δ_n and tangential displacement δ_s. There are two phases in the traction-displacement relation: (1) elastic phase, in which phase no damage occurred, and the traction increase linearly with the increase of displacement. (2) non-linear phase, the traction gradually decrease with the increase of displacement until the cohesive element completely losses the carrying capacity.

In elastic phase, the relation between traction and displacement can be expressed as

$$t_n = \bar{k}_n \bullet \delta_n, \quad t_s = \bar{k}_s \bullet \delta_s \tag{1}$$

Where $\bar{k}_n$, $\bar{k}_s$ is the initial normal/shear stiffness, the value of $\bar{k}_n$, $\bar{k}_s$ must be set in a reasonable range. The value of initial stiffness used in this paper is equal to 10^9 MPa/mm according to the work done by López *et al*. (2008).

Assuming there are only two kinds of damage modes in non-linear phase: tensile damage mode in normal direction and shear damage mode in tangential direction, the damage initiates when the following condition is met

$$\left(\frac{\langle t_n \rangle}{t_{n0}}\right)^2 + \left(\frac{t_s}{t_{s0}}\right)^2 \geq 1 \tag{2}$$

Where <> is the Macaulay bracket.

The bilinear damage model is adopted to express the relation between the traction and displacements in the non-linear phase as shown in Fig. 3.

The normal and tangential initial damage displacements δ_{n0}, δ_{s0} can be calculated through

$$\delta_{n0} = \frac{t_{n0}}{\bar{k}_n} \quad , \quad \delta_{s0} = \frac{t_{s0}}{\bar{k}_s} \tag{3}$$

The area under the curve in Fig. 3 stands for the normal/tangential fracture energy G_n/G_s, according to geometric relationship. The normal/tangential failure displacement δ_{nf}/δ_{sf} can be expressed as

$$\delta_{nf} = \frac{2G_n}{t_{n0}} \quad , \quad \delta_{sf} = \frac{2G_s}{t_{s0}} \tag{4}$$

When damage initiates, the displacements meet the square law similar to Eq. (2), assuming the displacements follow the same law when element is completely failure, the initial damage surface and failure surface which are illustrated in Fig. 4 can be expressed as

$$\begin{gathered} \left(\frac{\langle \delta_n \rangle}{\delta_{n0}}\right)^2 + \left(\frac{\delta_s}{\delta_{s0}}\right)^2 = 1 \\ \text{(initial damage surface)} \ , \\ \left(\frac{\langle \delta_n \rangle}{\delta_{nf}}\right)^2 + \left(\frac{\delta_s}{\delta_{sf}}\right)^2 = 1 \\ \text{(failure surface)} \end{gathered} \tag{5}$$

As shown in Fig. 4, the point B ($\delta_{n,\max}$, $\delta_{s,\max}$) is the historic maximum displacement point, where $\sqrt{\delta_{n,max}{}^2+\delta_{s,max}{}^2}$ is the historic maximum displacement during the loading process, and $\delta_{n,\max}$ ($\delta_{s,\max}$) is the normal (tangential) component of the historic maximum displacement. The point A ($\delta_{n,1}$, $\delta_{s,1}$) is the relative initial damage displacement point, which is obtained by finding the intersection point of vector OB and initial damage surface. The point C ($\delta_{n,2}$, $\delta_{s,2}$) is the relative failure displacement point, which is the intersection point of vector OB and the failure surface. The components of the point A and C can be calculated according to the geometric relationship in Fig. 4

$$\begin{gathered} \delta_{n1} = \frac{\langle \delta_n \rangle \delta_{n0} \delta_{s0}}{\sqrt{\delta_{n0}{}^2 \delta_s{}^2 + \langle \delta_n \rangle^2 \delta_{s0}{}^2}} \ , \\ \delta_{n2} = \frac{\langle \delta_n \rangle \delta_{nf} \delta_{sf}}{\sqrt{\delta_{nf}{}^2 \delta_s{}^2 + \langle \delta_n \rangle^2 \delta_{sf}{}^2}} \ , \\ \delta_{s1} = \frac{|\delta_s| \delta_{n0} \delta_{s0}}{\sqrt{\delta_{n0}{}^2 \delta_s{}^2 + \langle \delta_n \rangle^2 \delta_{s0}{}^2}} \ , \\ \delta_{s2} = \frac{|\delta_s| \delta_{nf} \delta_{sf}}{\sqrt{\delta_{nf}{}^2 \delta_s{}^2 + \langle \delta_n \rangle^2 \delta_{sf}{}^2}} \end{gathered} \tag{6}$$

So the relative displacement can be calculated by

$$\begin{gathered} \delta_{max} = \sqrt{\delta_{n,max}{}^2 + \delta_{s,max}{}^2} \ , \\ \delta_0 = \sqrt{\delta_{n1}{}^2 + \delta_{s1}{}^2} \ , \\ \delta_f = \sqrt{\delta_{n2}{}^2 + \delta_{s2}{}^2} \end{gathered} \tag{7}$$

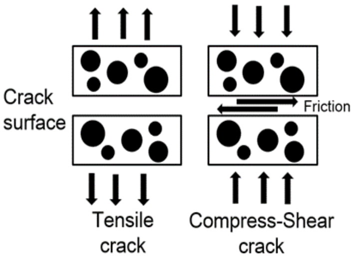

Fig. 5 The stress state of damaged area

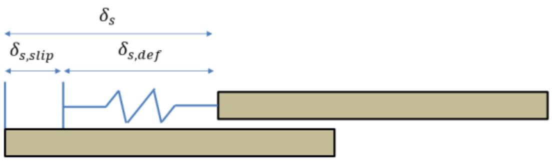

Fig. 6 The composition of total shear displacement

Where $\delta_{\max}$ is the historic maximum displacement during the loading process, δ_0 is the initial relative initial damage displacement, δ_f is the relative failure displacement.

According to the bilinear damage model, the definition of the damage factor D could be express as

$$D = \frac{(\delta_{max} - \delta_0)\delta_f}{(\delta_f - \delta_0)\delta_{max}} \tag{8}$$

So the normal/tangential stiffness during loading can be calculated according to

$$k_n = \begin{cases} (1-D)\bar{k}_n & \delta_n > 0 \\ \bar{k}_n & \delta_n \le 0 \end{cases}, \qquad k_s = (1-D)\bar{k}_s \tag{9}$$

The total shear stress during loading is composed of the shear stress in undamaged area and the frictional stress in damaged area as shown in Fig. 5. Especially, frictional stress only exist under the compression condition.

According to the friction law, the frictional stress in damaged area is equal to the shear stress caused by shear deformation $\delta_{s,def}$ before the shear stress reaching the maximal frictional stress $\tau_{\max}$, which means the damaged area can be considered as undamaged in this case. The maximal frictional stress $\tau_{\max}$ can be obtain with the coefficient of internal friction f

$$\tau_{\max} = f \bullet \langle -t_n \rangle = f \bullet \bar{k}_n \bullet \langle -\delta_n \rangle \tag{10}$$

The frictional stress in damaged area is equal to $\tau_{\max}$ if the shear stress caused by shear deformation is greater than $\tau_{\max}$, and the relative slip $\delta_{s,slip}$ occurs in this condition. So the total shear displacement δ_s in damaged area is composed of deformation displacement $\delta_{s,def}$ which cause the friction stress and $\delta_{s,slip}$ as in Fig. 6.

The frictional stress T_f in damaged area can be calculated according to

$$T_f = \begin{cases} \tau_{\max} \bullet \dfrac{\delta'_{s,def}}{\left|\delta'_{s,def}\right|} & \tau_{\max} \le \bar{k}_s \bullet \left|\delta'_{s,def}\right| \\ \bar{k}_s \bullet \delta'_{s,def} & \tau_{\max} > \bar{k}_s \bullet \left|\delta'_{s,def}\right| \end{cases} \tag{11}$$

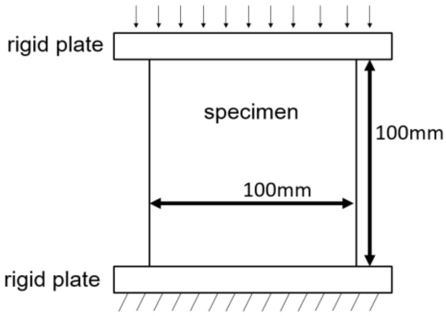

(a) The concrete specimen under uniaxial compression

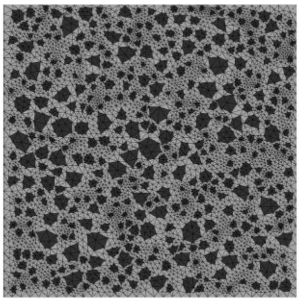

(b) The mesh of typical numerical sample

Fig. 7 Numerical model tests

Where $\delta'_{s,def}$ is the shear deformation, which can be obtained with δ_s and $\delta_{s,slip}$ (not updated):

$$\delta'_{s,def} = \delta_s - \delta_{s,slip} \tag{12}$$

The relative slip $\delta_{s,slip}$ should be updated after the calculation of T_f according to the geometric relationship in Fig. 6

$$\delta_{s,slip} = \delta_s - \frac{\tau_{\max}}{\bar{k}_s} \quad (\tau_{\max} \le \bar{k}_s \bullet \left|\delta'_{s,def}\right|) \tag{13}$$

The traction is composed of the stress in the damaged area and undamaged area, so the normal stress t_n and the tangential stress t_s can be calculated according to

$$\begin{cases} t_n = k_n \delta_n \\ t_s = k_s \delta_s + D \bullet T_f \end{cases} \tag{14}$$

4. Results and analysis

Uniaxial compression tests of 100 mm×100 mm numerical specimens were modelled in this study (Fig. 7(a)). All the models were placed between two rigid plates, the plate below the specimen was fixed and the plate above was subjected to a uniform displacement loading. Friction exists between the surface of the concrete and the rigid plate, the friction coefficient of the interface of the concrete and the plate under low friction condition (LF condition) is 0.001 and the one under high friction condition (HF condition) is 0.25. All tests were ended as a displacement d=1 mm (ε=0.01).

Triangular solid elements of aggregates and mortar were assumed with linear behavior. The constitutive presented in this study were used in the cohesive elements. As the weakest region (without considering the pores and initial cracks) in concrete, the mechanical properties of the ITZ are very important to this study. Due to the difficulty to determine the local mechanical of the ITZ with the existing measurement techniques (Scrivener *et al*. 2004, Mondal *et al*. 2009), the researchers mainly adopted empirical material parameters to characterize the mechanical behavior of the ITZ (Setiawan *et al*. 2017, Yu *et al*. 2018, Pan *et al*. 2018, Zhang *et al*. 2018). In terms of mechanical properties, ITZ is normally considered as a weakened mortar. According to the existing researches (López *et al*. 2008a, b, Kim and Al-Rub 2011, Nitka and Tejchman 2015, Shen *et al*. 2015, Wang *et al*. 2016, Peng *et al*. 2019), the ratio of material parameters between ITZ and mortar is normally be set as 0.5~0.8. According to the work done (López *et al*.2008a, b, Wang *et al*. 2016) with the similar model, the ratio adopted in this paper is 0.5.

Based on the similar research works (López *et al.* 2008a, b, Wang *et al.* 2016) and repeated trial calculations, the material parameters used in this study are: E=60 GPa (aggregate), E=25 GPa (mortar) and v=0.2(both) for solid elements; $\bar{k}_n = \bar{k}_s = 10^9$ MPa/m, t_{n0}=1.5 MPa, t_{s0}=5.25 MPa, G_n=40 N/m, G_s=10 G_n, f=0.45 for the cohesive elements of the ITZ; $\bar{k}_n = \bar{k}_s = 10^9$ MPa/m, t_{n0}=3 MPa, t_{s0}=10.5 MPa, G_n=80 N/m, G_s=10 G_n for the mortar-mortar cohesive elements; for the aggregate-aggregate cohesive elements, the linear elastic behavior were used: $\bar{k}_n = \bar{k}_s = 10^9$ MPa/m.

A series of simulations were conducted to investigate the effects of key parameters on the statistical response of numerical specimens. The numerical specimens using the polygon aggregates with P_{agg}=32% as mentioned in Table.1. For each group of tests, 5 samples were modelled and analysed to reduce the accident error. The typical numerical sample and its mesh with average element size=1 mm is shown in Fig. 7(b). All numerical samples were calculated using ABAQUS/Explicit solver with user subroutine VUMAT based on the constitutive presented in this study.

4.1 Typical compression failure behavior of concrete

The basic results obtained are shown in Figs. 8-10. In Fig. 8, the resulting average stress-strain curve under LF condition and HF condition is depicted, together with experimental results of Van Vliet and Van Mier (1996). The detailed of crack evolution at various loading stages under LF condition (marks A, B, C in Fig. 8) and under HF condition (marks D, E, F in Fig. 8) are represented in Figs. 9-10. The cracks in those plots are marked in red, and the final deformed shape of the model are shown in Fig. 9(d) and Fig. 10(d).

The stress-strain curve under LF and HF condition (Fig. 8) is similar to the experimental one, with a sharp initial post-peak drop and a long horizontal tail under LF condition, and a gentle post-peak descending segment under HF condition.

The stress-strain curve under LF and HF condition (Fig. 8) is similar to the experimental one, with a sharp initial post-peak drop and a long horizontal tail under LF condition, and a gentle post-peak descending segment under HF condition.

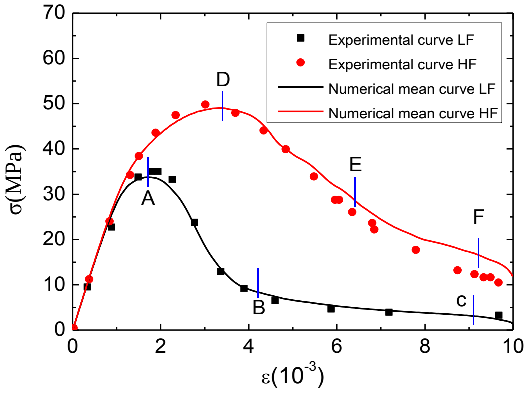

Fig. 8 Average stress-strain curve under compression condition

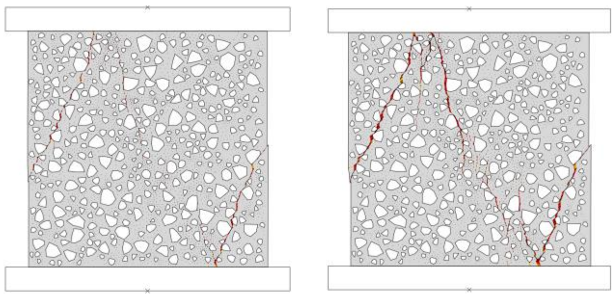

(a) Loading stage A in Fig. 8 (b) Loading stage B in Fig. 8

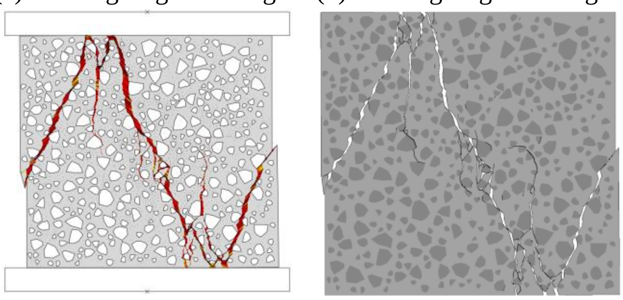

(c) Loading stage C in Fig. 8 (d) Final deformed shape

Fig. 9 typical fracture process of concrete under LF condition

As shown in Fig. 9, micro cracks started developing by ripping through the loading surfaces (top and bottom surface) and ITZ. The cracks and the loading direction form a slight angle. The micro cracks were continually opening and getting separated during the loading process. At final stage, the main crack eventually cut through the middle part, two sides of specimen perpendicular to the loading direction. The loading surfaces finally were cut through by several cracks.

Fig. 10 shows how micro cracks initiated and developed under HF condition. Unlike LF condition, micro cracks started from left and right sides of specimen. The loading surfaces were relatively complete during the fracture process, and the crack opening degree was smaller than the one under LF condition due to the limiting friction effect of the loading surfaces.

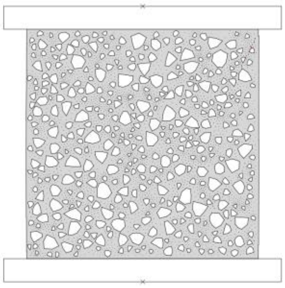

(a) Loading stage D in Fig. 8

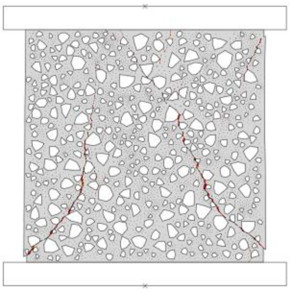

(b) Loading stage E in Fig. 8

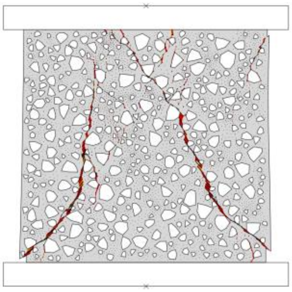

(c) Loading stage F in Fig. 8

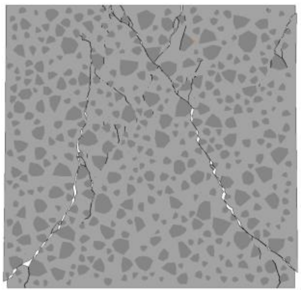

(d) Final deformed shape

Fig. 10 Typical fracture process of concrete under HF condition

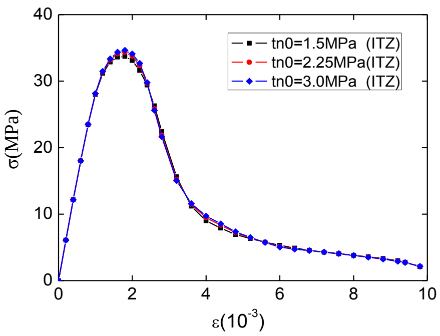

(a) Average stress-strain curve (ITZ)

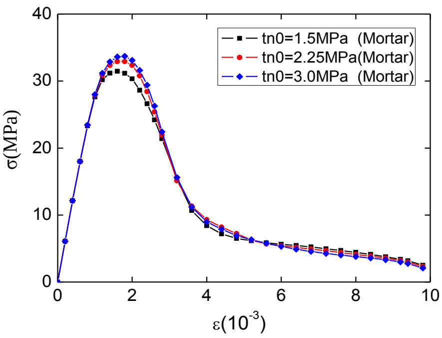

(b) Average stress-strain curve (Mortar)

Fig. 11 The influence of tensile strength on the compression mechanical behavior

4.2 Influence of tensile and shear strength

To investigate the influence of the tensile strength t_{n0} and shear strength t_{s0}, a series of numerical samples were analyzed with different tensile strength (1.5 MPa, 2.25 MPa, 3.0 MPa) and shear strength (5.25 MPa, 7.88 MPa, 10.5 MPa) respectively. The effect of tensile strength t_{n0} of ITZ and mortar-mortar interfaces were shown in Fig. 11. It can be seen that the compression mechanical behavior of concrete is hardly affected by the tensile strength, and the tensile strength of the mortar-mortar interfaces has a larger effect than the one of the ITZ on the compression mechanical behavior of concrete. This is because the load capacity of concrete under compression condition is mainly depended on the shear strength and friction of concrete.

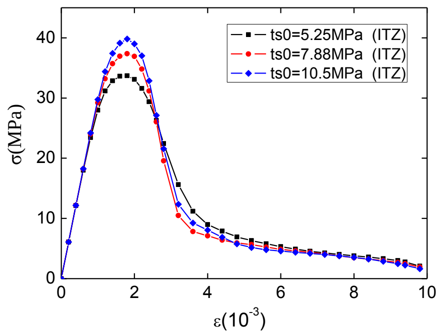

(a) Average stress-strain curve (ITZ)

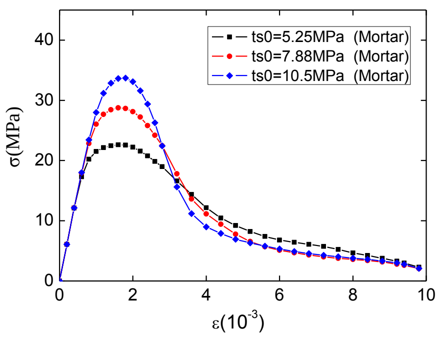

(b) Average stress-strain curve (Mortar)

Fig. 12 The influence of shear strength on the compression mechanical behavior

The effect of the shear strength t_{s0} of ITZ and mortar-mortar interfaces were shown in Fig. 12. It can be seen that the load capacity of concrete under compression condition is sensitive to the shear strength. Like the tensile strength, the load capacity is more sensitive to the shear strength of mortar-mortar interfaces than the one of ITZ. It indicates that the mechanical behavior of concrete under compression condition is mainly determined by the mechanical behavior of mortar.

4.3 Influence of inner friction coefficient

The influence of the inner friction coefficient f was investigated by analysing the samples with different f (0.25, 0.35, 0.45, and 0.55) under LF condition. The micro cracks distribution of different f at final stage are shown in Fig. 13. It can be seen that the numbers of micro cracks decreases with the increase of the inner friction coefficient f. It means that micro cracks of concrete are easier to develop with the lower f under compression condition, because the constraints caused by inner friction become smaller.

It is noteworthy that the inner friction coefficient f basically has no effect on the tensile strength of samples. Fig. 15(a) compares the stress-strain curve for 4 different f.

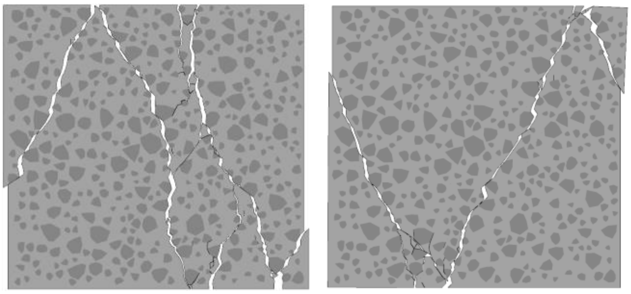

(a) *f*=0.25 (b) *f*=0.35

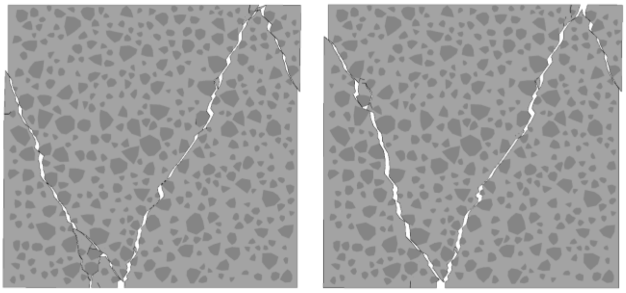

(c) *f*=0.45 (d) *f*=0.55

Fig. 13 The concrete fracture pattern of different *f* under LF condition

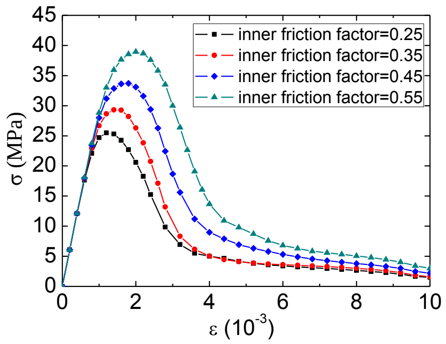

(a) Average stress-strain curve

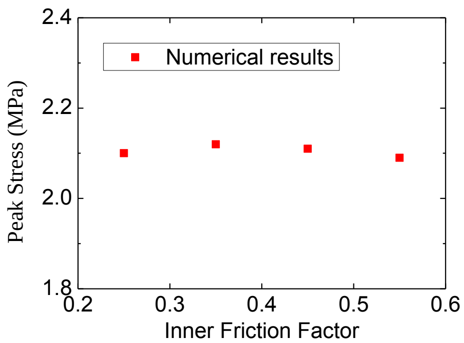

(b) Average peak stress

Fig. 14 The influence of *f* on compression mechanical

It can be seen that the tensile strength remains unchanged with the increasing of *f* in Fig. 15(b). This is because the stress between the cracks under tensile condition is mainly tensile and shear stress. So the friction is basically non-existent between the cracks without the compression stress. Fig. 16 shows the typical crack pattern of samples under the tensile condition: the main crack run through the sample perpendicular to the loading direction.

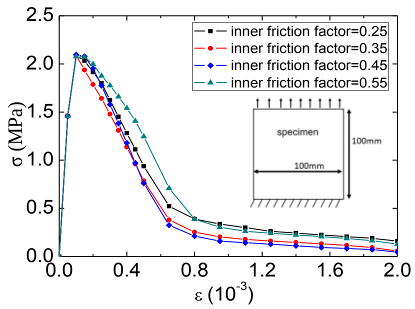

(a) Average stress-strain curve

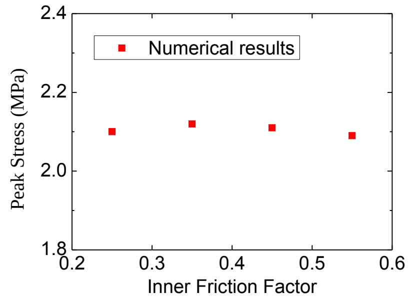

(b) Average peak stress

Fig. 15 The influence of *f* on tensile mechanical behavior

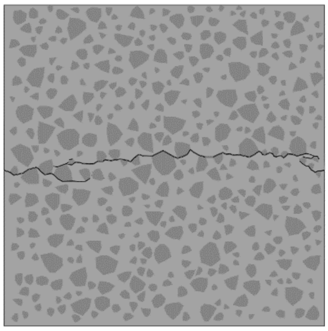

Fig. 16 Typical tensile fracture pattern of concrete

4.4 Influence of specimen size

Simulations under LF condition and HF condition with three different specimen size from 100 mm×100 mm to 200 mm×200 mm were carried out, all simulations were ended in ε=0.01 for analysis. Fig. 17 shows the numerical samples with three different size.

The typical fracture patterns of three different cubic size under LF condition are shown in Fig. 18. The fracture patterns are similar to the one in Fig. 9 with micro cracks all ripping through the loading surfaces, middle part and left/right sides of specimens, but the number of cracks increases with the increasing of cubic size. Fig. 19 shows the stress-strain curves of different cubic size. It can be seen that the compression strength and pre/post peak behavior are similar. It means that the cubic size influences the concrete fracture pattern but basically has no effect on the compression mechanical behavior of concrete under LF condition.

Fig. 20 shows the typical fracture patterns under HF condition: unlike LF condition, the cracks mainly happened at the left/right side of specimens due to the friction

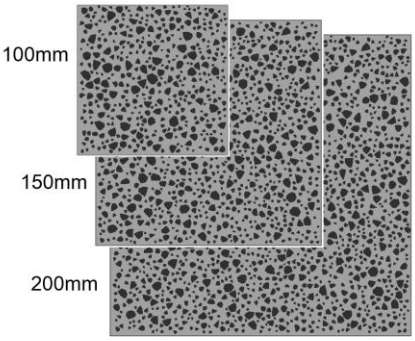

Fig. 17 Numerical samples with three different size

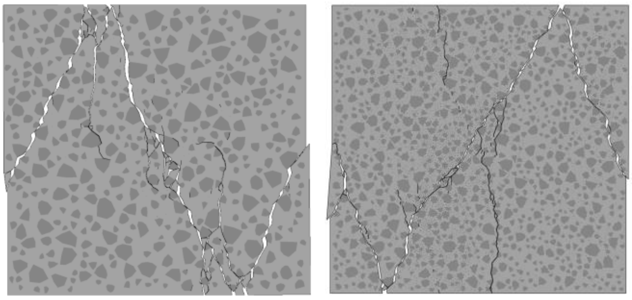

(a) Size 100×100 mm (b) Size 150×150 mm

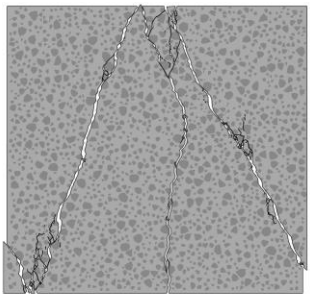

(c) Size 200×200 mm

Fig. 18 The concrete fracture pattern of different size under LF condition

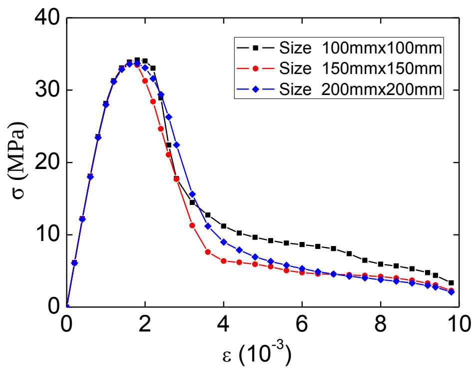

Fig. 19 Average stress-strain curve of different size under LF condition

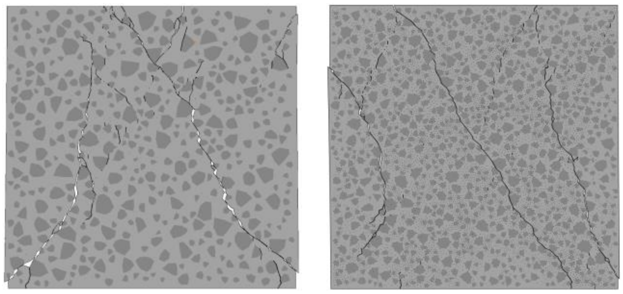

(a) Size 100×100 mm (b) Size 150×150 mm

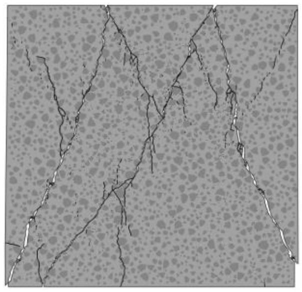

(c) Size 200×200 mm

Fig. 20 The concrete fracture pattern of different size under HF condition

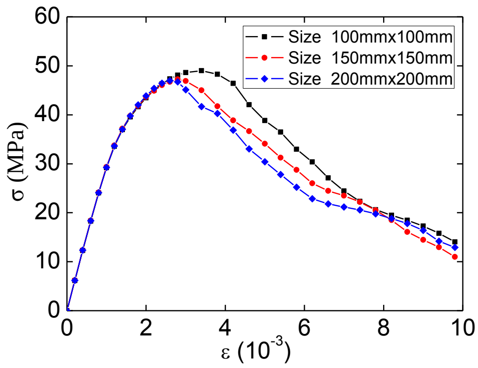

Fig. 21 Average stress-strain curve of different size under HF condition

constraint of the loading surfaces. The number of cracks and cracks open degree increase with the increase of specimen size. The stress-strain curves under HF condition are shown in Fig. 21. The strength of small size is higher than the one with larger size, and the peak strain increases with the decreasing of specimen size. This is because the loading surfaces with larger specimen size has smaller constraint effect on the cracks development of specimen.

4.5 Influence of aggregate volume fraction

The influence of aggregate volume fraction P_{agg} on compression behavior is investigated by analyzing the samples with different P_{agg} from 22% to 42%. The final fracture patterns of specimens with different P_{agg} under LF and HF condition are compared in Fig. 22. It clearly shows that, as aggregate volume fraction increased, the number of micro cracks increases under LF and HF condition. This is because the region of ITZ increases with the increase of P_{agg} , and it makes the cracks easier to develop by passing through ITZ.

Fig. 23 depicts the average stress-strain curves, the results shows that as P_{agg} increased, the compression strength and peak strain decreases slightly, but post peak drop become flatter. It is because the higher P_{agg} makes more region of ITZ with lower tensile/shear capacity, which

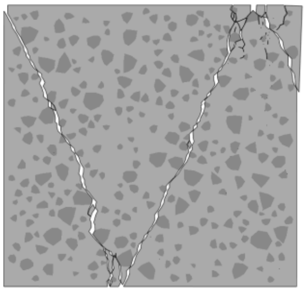
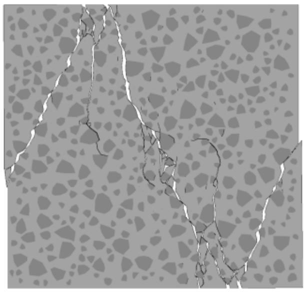
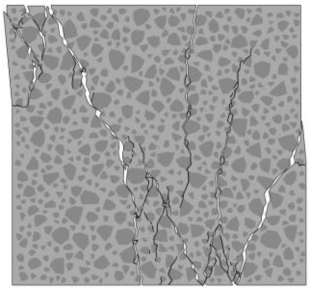

(a) P_{agg}=22% (LF condition) (b) P_{agg}=32% (LF condition) (c) P_{agg}=42% (LF condition)

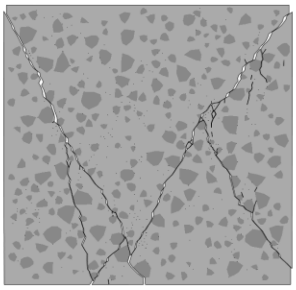
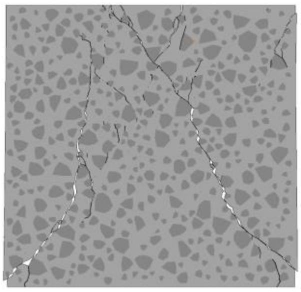
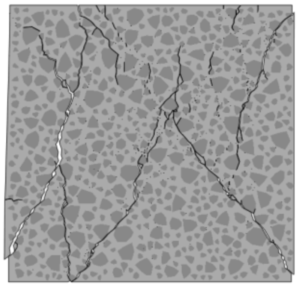

(d) P_{agg}=22% (HF condition) (e) P_{agg}=32% (HF condition) (f) P_{agg}=42% (HF condition)

Fig. 22 The concrete fracture pattern of different P_{agg}

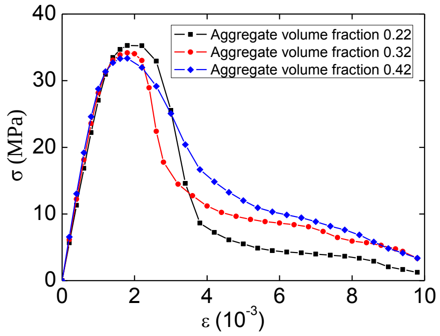

(a) LF condition

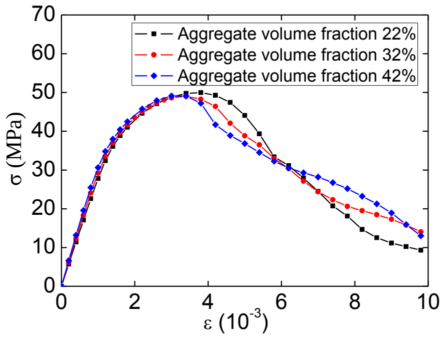

(b) HF condition

Fig. 23 Average stress-strain curve of different P_{agg}:

cause the decrease of cohesive in the concrete.

5. Conclusions

Numerical models of concrete with random polygon aggregate and constitutive relation governing the cohesive element have been developed in this study. The fracture process was simulated by ABAQUS with subroutine vumat. The influences of key parameters on concrete compression mechanical characteristic are analyzed. The main conclusion are:

(1) The friction between the concrete surface and loading plate has a significant influence on the compression character and fracture pattern of concrete. So it is important to consider the surface friction effect when analyzing the compression problem.

(2) Concrete compression bearing capacity is highly sensitive to the shear strength (ITZ and mortar-mortar interfaces) and inner friction coefficient. The strength of mortar-mortar interfaces has a larger effect on concrete compression mechanical behavior than the one of ITZ. Furthermore, there is a linear relationship between compression strength and inner friction coefficient under LF condition.

(3) Compared with the surficial friction effect and material parameters, the mesostructure of concrete (cubic size, aggregate content) has a small influence on the compressive strength of concrete. However, the fracture pattern is sensitive to the mesostructure.

In this study, a 2D model with the modified constitutive has been applied in the simulation of concrete fracture process under compressive condition. Although the fracture pattern and mechanical behavior obtained shows reasonable, the 2D model still remains limited to solve the planar problem. The further study via 3D model is required and ongoing to solve the more complex problems such as the multiaxial compression problem.

Acknowledgements

This study was funded by the State Key Program of National Natural Science of China (Grant no. 51739008), the National Major Scientific Instruments Development

Project of China (Grant no.51527811), and the Postgraduate Research & Practice Innovation Program of Jiangsu Province(Grant no.2018B683X14).

References

Caballero, A., López, C.M. and Carol, I. (2006), "3D meso-structural analysis of concrete specimens under uniaxial tension", *Comput. Meth. Appl. Mech. Eng.*, **195**(52), 7182-7195. http://dx.doi.org/10.1016/j.cma.2005.05.052.

Chen, G., Hao, Y.F. and Hao, H. (2015), "3D meso-scale modelling of concrete material in spall tests", *Mater. Struct.*, **48**(6), 1887-1899. http://dx.doi.org/10.1617/s11527-014-0281-z.

Du, C.B. and Sun, L.G. (2007), "Numerical simulation of aggregate shapes of two-dimensional concrete and its application", *J. Aerosp. Eng.*, **20**(3), 172-178. https://doi.org/10.1061/(ASCE)0893-1321(2007)20:3(172).

Du, X.L., Jin, L. and Ma, G.W. (2013a), "Macroscopic effective mechanical properties of porous dry concrete", *Cement Concrete Res.*, **44**, 87-96. http://dx.doi.org/10.1016/j.cemconres.2012.10.012.

Du, X.L., Jin, L. and Ma, G.W. (2013b), "Meso-element equivalent method for the simulation of macro mechanical properties of concrete", *Int. J. Damage Mech.*, **22**(5), 617-642. http://dx.doi.org/10.1177/1056789512457096.

Gao, Z.G. and Liu, G.T. (2003), "Two-dimensional random aggregate structure for concrete", *J. Tsinghua Univ. (Sci. Technol.)*, **43**(5), 710-714. https://doi.org/10.3321/j.issn:1000-0054.2003.05.036.

Grassl, P., Grégoire, D., Solano, L.R. and Pijaudier-Cabot, G. (2012), "Meso-scale modelling of the size effect on the fracture process zone of concrete", *Int. J. Solid. Struct.*, **49**(13), 1818-1827. http://dx.doi.org/10.1016/j.ijsolstr.2012.03.023.

Guan, X., Zhao, S. and Liu, J. (2018), "Surgically inspired technique of ITZ integration in lattice model for numerical simulation of cement composites", *KSCE J. Civil Eng.*, **22**(11), 4454-4460. http://dx.doi.org/10.1007/s12205-018-0966-x.

Haeri, H. and Sarfarazi, V. (2016), "Numerical simulation of tensile failure of concrete using particle flow code (PFC)", *Comput. Concrete*, **18**(1), 39-51. http://dx.doi.org/10.12989/cac.2016.18.1.039.

Haeri, H., Sarfarazi, V., Zhu, Z. and Marji, M.F. (2018), "Simulating the influence of pore shape on the Brazilian tensile strength of concrete specimens using PFC2D", *Comput. Concrete*, **22**(5), 469-479. http://dx.doi.org/10.12989/cac.2018.22.5.469.

Jin, L, Yu W.X., Du, X.L., Zhang, S. and Li, D. (2019), "Meso-scale modelling of the size effect on dynamic compressive failure of concrete under different strain rates", *Int. J. Impact Eng.*, **125**, 1-12. https://doi.org/10.1016/j.ijimpeng.2018.10.011.

Jin, L., Du, X.L. and Ma, G.W. (2012), "Macroscopic effective moduli and tensile strength of saturated concrete", *Cement Concrete Res.*, **42**(12), 1590-1600. http://dx.doi.org/10.1016/j.cemconres.2012.09.012.

Karavelić, E., Nikolić, M., Ibrahimbegovic, A. and Kurtović, A. (2019), "Concrete meso-scale model with full set of 3D failure modes with random distribution of aggregate and cement phase. Part I: Formulation and numerical implementation", *Comput. Meth. Appl. Mech. Eng.*, **344**, 1051-1072. http://dx.doi.org/10.1016/j.cma.2017.09.013.

Kim, S.M. and Al-Rub, R.K.A. (2011), "Meso-scale computational modeling of the plastic-damage response of cementitious composites", *Cement Concrete Res.*, **41**(3), 339-358. https://doi.org/10.1016/j.cemconres.2010.12.002.

Li, X. and Chen, J. (2017), "An extended cohesive damage model for simulating arbitrary damage propagation in engineering materials", *Comput. Meth. Appl. Mech. Eng.*, **315**, 744-759. http://dx.doi.org/10.1016/j.cma.2016.11.029.

Lilliu, G. and Van Mier, J.G. (2003), "3D lattice type fracture model for concrete", *Eng. Fract. Mech.*, **70**(7-8), 927-941. http://dx.doi.org/10.1016/S0013-7944(02)00158-3.

López, C.M., Carol, I. and Aguado, A. (2008a), "Meso-structural study of concrete fracture using interface elements. I: numerical model and tensile behavior", *Mater. Struct.*, **41**(3), 583-599. http://dx.doi.org/10.1617/s11527-007-9314-1.

López, C.M., Carol, I. and Aguado, A. (2008b), "Meso-structural study of concrete fracture using interface elements. II: compression, biaxial and Brazilian test", *Mater. Struct.*, **41**(3), 601-620. http://dx.doi.org/10.1617/s11527-007-9312-3.

Mohamed, A.R. and Hansen, W. (1999), "Micromechanical modeling of concrete response under static loading-Part 1: model development and validation", *Mater. J.*, **96**(2), 196-203. http://dx.doi.org/10.14359/445.

Mondal, P., Shah, S.P. and Marks, L.D. (2009), "Nanomechanical properties of interfacial transition zone in concrete", Eds. Z. Bittnar., P.M. Bartos., J. Němeček., V Šmilauer. and J. Zeman, *Nanotechnology in Construction 3*, Springer, Berlin, Heidelberg. http://dx.doi.org/10.1007/978-3-642-00980-8_42.

Nguyen, T.T., Bui, H.H., Ngo, T.D., Nguyen, G.D., Kreher, M.U. and Darve, F. (2019), "A micromechanical investigation for the effects of pore size and its distribution on geopolymer foam concrete under uniaxial compression", *Eng. Fract. Mech.*, **209**, 228-244. http://dx.doi.org/10.1016/j.engfracmech.2019.01.033.

Nitka, M. and Tejchman, J. (2015), "Modelling of concrete behaviour in uniaxial compression and tension with dem", *Granular Matter.*, **17**(1), 145-164. http://dx.doi.org/10.1007/s10035-015-0546-4.

Ooi, E.T. and Yang, Z.J. (2011), "Modelling crack propagation in reinforced concrete using a hybrid finite element–scaled boundary finite element method", *Eng. Fract. Mech.*, **78**(2), 252-273. http://dx.doi.org/10.1016/j.engfracmech.2010.08.002.

Pan, Z., Wang, D., Ma, R. and Chen, A. (2018), "A study on ITZ percolation threshold in mortar with ellipsoidal aggregate particles", *Comput. Concrete*, **22**(6), 551-561. http://dx.doi.org/10.12989/cac.2018.22.6.551.

Peng, Y., Wang, Q., Ying, L., Kamel, M. and Peng, H. (2019), "Numerical simulation of dynamic mechanical properties of concrete under uniaxial compression", *Mater.*, **12**(4), 643. https://doi.org/10.3390/ma12040643.

Rangari, S., Murali, K. and Deb, A. (2018), "Effect of meso-structure on strength and size effect in concrete under compression", *Eng. Fract. Mech.*, **195**, 162-185. http://dx.doi.org/10.1016/j.engfracmech.2018.04.006.

Roth, S.N., Léger, P. and Soulaïmani, A. (2015), "A combined XFEM–damage mechanics approach for concrete crack propagation", *Comput. Meth. Appl. Mech. Eng.*, **283**, 923-955. http://dx.doi.org/10.1016/j.cma.2014.10.043.

Scrivener, K.L., Crumbie, A.K. and Laugesen, P. (2004), "The interfacial transition zone (ITZ) between cement paste and aggregate in concrete", *Interf. Sci.*, **12**(4), 411-421. http://dx.doi.org/10.1023/B:INTS.0000042339.92990.4c.

Setiawan, Y., Gan, B.S. and Han, A.L. (2017), "Modeling of the ITZ zone in concrete: Experiment and numerical simulation", *Comput. Concrete*, **19**(6), 641-649. https://doi.org/10.12989/cac.2017.19.6.641.

Shen, L., Ren, Q.W, Xia, N., Sun, L.G. and Xia, X.Z. (2015), "Mesoscopic numerical simulation of effective thermal conductivity of tensile cracked concrete", *Constr. Build. Mater.*, **95**, 467-475. http://dx.doi.org/10.1016/j.conbuildmat.2015.07.117.

Snozzi, L., Caballero, A. and Molinari, J.F. (2011), "Influence of the meso-structure in dynamic fracture simulation of concrete under tensile loading", *Cement Concrete Res.*, **41**(11), 1130-1142. http://dx.doi.org/10.1016/j.cemconres.2011.06.016.

Van Mier, J.G., Van Vliet, M.R. and Wang, T.K. (2002), "Fracture mechanisms in particle composites: statistical aspects in lattice type analysis", *Mech. Mater.*, **34**(11), 705-724. http://dx.doi.org/10.1016/S0167-6636(02)00170-9.

Van Vliet, M.A. and Van Mier, J.M. (1996), "Experimental investigation of concrete fracture under uniaxial compression", *Mech. Cohesive-frictional Mater.*, **1**(1), 115-127. http://dx.doi.org/10.1002/(SICI)1099-1484(199601)1:1<115::AID-CFM6>3.0.CO;2-U.

Wang, G.L., Pekau, O.A., Zhang, C.H. and Wang, S.M. (2000), "Seismic fracture analysis of concrete gravity dams based on nonlinear fracture mechanics", *Eng. Fract. Mech.*, **65**(1), 67-87. http://dx.doi.org/10.1016/S0013-7944(99)00104-6.

Wang, X.F., Yang, Z.J., Yates, J.R., Jivkov, A.P. and Zhang, C. (2015), "Monte Carlo simulations of mesoscale fracture modelling of concrete with random aggregates and pores", *Constr. Build. Mater.*, **75**, 35-45. http://dx.doi.org/10.1016/j.conbuildmat.2014.09.069.

Wang, X.F., Zhang, M.Z. and Jivkov, A.P. (2016), "Computational technology for analysis of 3D meso-structure effects on damage and failure of concrete", *Int. J. Solid. Struct.*, **80**, 310-333. http://dx.doi.org/10.1016/j.ijsolstr.2015.11.018.

Wriggers, P. and Moftah, S.O. (2006), "Mesoscale models for concrete: Homogenisation and damage behavior", *Finite Elem. Anal. Des.*, **42**(7), 623-636. http://dx.doi.org/10.1016/j.finel.2005.11.008.

Yang, Z.J., Su, X.T., Chen, J.F. and Liu, G.H. (2009), "Monte Carlo simulation of complex cohesive fracture in random heterogeneous quasi-brittle materials", *Int. J. Solid. Struct.*, **46**(17), 3222-3234. http://dx.doi.org/10.1016/j.ijsolstr.2009.04.013.

Yu, Q., Liu, H., Yang, T. and Liu, H. (2018), "3D numerical study on fracture process of concrete with different ITZ properties using X-ray computerized tomography", *Int. J. Solid. Struct.*, **147**, 204-222. https://doi.org/10.1016/j.ijsolstr.2018.05.026.

Zhang, C., Zhou, W., Ma, G., Hu, C. and Li, S. (2015), "A meso-scale approach to modeling thermal cracking of concrete induced by water-cooling pipes", *Comput. Concrete*, **15**(4), 485-501. http://dx.doi.org/10.12989/cac.2015.15.4.485.

Zhang, S., Zhang, C., Liao, L. and Wang, C. (2018), "Numerical study of the effect of ITZ on the failure behaviour of concrete by using particle element modelling", *Constr. Build. Mater.*, **170**, 776-789. https://doi.org/10.1016/j.conbuildmat.2018.03.040.

CC